Dalton Transactions

PAPER

View Article Online
View Journal | View Issue

Cite this: *Dalton Trans.*, 2016, **45**, 16290

Effect of dopant concentration on visible light driven photocatalytic activity of $Sn_{1-x}Ag_xS_2$

Xiaodan Cui,[a] Wangwang Xu,[a] Zhiqiang Xie,[a] James A. Dorman,[b] Maria Teresa Gutierrez-Wing[c] and Ying Wang*[a]

Received 15th July 2016,
Accepted 9th September 2016

DOI: 10.1039/c6dt02812h

www.rsc.org/dalton

Tin(IV) sulfide (SnS_2), as a mid-band-gap semiconductor shows good potential as an excellent photocatalyst due to its low cost, wide light spectrum response and environment-friendly nature. However, to meet the demands of large-scale water treatment, a SnS_2 photocatalyst with a red-shifted band gap, increased surface area and accelerated molecule and ion diffusion is required. Doping is a facile method to manipulate the optical and chemical properties of semiconductor materials simultaneously. In this work, SnS_2 photocatalysts with varied Ag doping content are synthesized through a facile one-step hydrothermal method. The product is characterized by XRD, SEM, TEM and UV-Vis spectrometry. The photocatalytic activity of the as-prepared $Sn_{1-x}Ag_xS_2$ is studied by the degradation of methylene blue (MB) dye under solar light irradiation. It is found that increasing the Ag dopant concentration can effectively increase the solar light adsorption efficiency of the photocatalyst and accelerate heterogeneous photocatalysis. The optimal concentration of Ag dopant is found to be 5% with the highest rate constant being 1.8251 $hour^{-1}$. This study demonstrates that an optimal amount of Ag doping can effectively increase the photocatalytic performance of SnS_2 and will promote the commercialization of such photocatalysts in the photocatalytic degradation of organic compounds.

1. Introduction

Due to the fast development of science and technology, environmental deterioration has become an emergent problem worldwide in recent decades. In particular organic dyes, which exist in all kinds of articles of daily use by humans, have become one of the most serious water pollutants. According to the literature, ~12% of industrial dyes that are highly cytotoxic to living bodies[1,2] and difficult to degrade naturally,[3] leach out in the dyeing process, and ~20% of the dyes are disposed of into waste water effluents.[4] Therefore, developing a semiconductor photocatalyst to satisfy the increasing demand for environment remediation has attracted tremendous attention. Currently, TiO_2 is the most commonly used photocatalyst for dye degradation, due to its low cost, eco-friendly nature, good stability and high catalytic activity.[5–8] However, limited by its wide bandgap (3.2 eV), TiO_2 can only respond to ultraviolet light (λ < 390 nm), which only accounts for a small amount of sunlight.

Recently, many efforts have been devoted to developing semiconducting transition-metal sulfides as visible-light driven photocatalysts, owing to their mid-band-gap properties and high activity in the visible to near-infrared regions.[9,10] Among these materials, CdS stands out due to its unique optical properties with a band gap of 2.4 eV, but its hazards to human health hinder its further development. Compared with TiO_2 and CdS, SnS_2 shows good potential as an excellent photocatalyst due to its low toxicity, low cost, wide light spectrum response and good chemical stability. Hence, this compound has found wide application in many fields, including lithium ion batteries,[11] solar cells[12,13] and photocatalysts.[14,15] For example, Li *et al.* developed SnS_2/TiO_2 nanocomposites that displayed excellent photocatalytic activity and good stability;[16] Yu *et al.* reported a SnS_2 nanosheet photocatalyst that exhibited much higher photocatalytic H_2 evolution activity than P25-TiO_2.[14] However, to meet the demands of large-scale water treatment, SnS_2 photocatalysts with superior optical and electrical properties are required.

To improve the performance of a semiconductor material, a band gap shift to the visible to near-infrared regions, an increase in the surface area to volume ratio, accelerated molecule and ion diffusion, and avoiding electron–hole recombination, are all favorable strategies.[17–21] Among various techniques, doping with metal ions has proven to be a facile

[a]*Department of Mechanical & Industrial Engineering, Louisiana State University, Baton Rouge, LA 70803, USA. E-mail: ywang@lsu.edu; Fax: +1-225-578-9162; Tel: +1225-578-8577*
[b]*Department of Chemical Engineering, Louisiana State University, Baton Rouge, LA 70803, USA*
[c]*Louisiana Sea Grant/School of Renewable Natural Resources, Louisiana State University, Baton Rouge, LA 70803, USA*

method to manipulate the optical and chemical properties of semiconductor materials simultaneously, and to modify their crystallinity and morphologies as well.[12,22,23] It has been reported that a certain amount of extrinsic impurities can efficiently narrow the band gap, reduce the particle size, facilitate mass diffusion and serve as electron/hole trap centers as well. Recently, silver has attracted much attention as a dopant for photocatalysts due to the antibacterial nature of silver and silver ions.[24] In addition, the Ag dopant has been reported to effectively trap excited electrons and red shift the optical response.[25] Thus, through partially substituting Sn with Ag, the photocatalytic activity of SnS_2 is expected to improve.

In this study, a $Sn_{1-x}Ag_xS_2$ photocatalyst is synthesized through a simple one-step hydrothermal method with a varied Ag doping amount. The effects of the dopant on the crystallinity and morphology are explored *via* XRD, SEM and TEM. The photocatalytic activity of the as-prepared $Sn_{1-x}Ag_xS_2$ nanoparticles is studied by the degradation of methylene blue (MB) dye under solar light irradiation. Moreover, the effect of the dopant concentration on the visible light driven photocatalytic activity is investigated by varying the Ag doping concentration from 1% to 7%. Due to the defects introduced by the Ag dopant, the as-prepared $Sn_{1-x}Ag_xS_2$ demonstrates significantly improved photocatalytic activity compared to pristine SnS_2. In addition, the photocatalytic activity of $Sn_{1-x}Ag_xS_2$ is optimized by tuning the dopant concentration, and it is observed that the $Sn_{0.95}Ag_{0.05}S_2$ photocatalyst shows the highest performance. These results indicate that a proper amount of Ag doping can effectively red shift the band gap, increase the surface area and facilitate the mass diffusion of SnS_2 which will promote the commercialization of the photocatalyst in the photocatalytic degradation of organic pollutants.

2. Experimental

2.1 $Sn_{1-x}Ag_xS_2$ synthesis

$Sn_{1-x}Ag_xS_2$ photocatalysts were synthesized using a facile solvothermal method. 24 mM of tin(IV) chloride pentahydrate, 110 mM of thioacetamide, 1.2 mM sodium dodecyl sulfate as a surfactant and silver nitrate were dissolved into ethylene glycol under magnetic stirring. The molar concentration of silver nitrate was set to be 0.01, 0.03, 0.05 and 0.07 with respect to tin(IV) chloride pentahydrate. The respective samples were labeled as $Sn_{1-x}Ag_xS_2$ (x = 0.01, 0.03, 0.05 and 0.07). After stirring for 30 min, the obtained mixture was then poured into a stainless steel Teflon-lined autoclave. The autoclave was heated to 180 °C. After 24 hours, the autoclave was cooled to room temperature naturally. Then the precipitate was washed with DI water and ethanol several times. For comparison purposes, pristine SnS_2 was synthesized without adding silver nitrate using the same method.

2.2 Characterizations

The crystallinity of pristine SnS_2 and $Sn_{1-x}Ag_xS_2$ with different silver concentrations was studied by X-ray diffraction (XRD) using a Rigaku MiniFlex diffractometer with Cu Kα radiation operated at 30 kV and 15 mA with a scan rate of 2° min^{-1}. The morphologies of the nanoparticles were demonstrated by an FEI Quanta 3D FEG scanning electron microscope (SEM) at an accelerating voltage of 20 kV. High-resolution transmission electron microscopy (HRTEM) images of $Sn_{1-x}Ag_xS_2$ were taken using a JEOL HRTEM (JEM-1400) electron microscope with an acceleration voltage of 120 kV. The UV-Vis absorbance spectra were measured by a Perkin-Elmer Lambda 900 system with an integrating sphere from 800 to 300 nm at 1 nm intervals and with a 0.2 s dwell time. A tungsten lamp was used for excitation with the wavelength selected with a dual monochromator system and the spectra were collected with a photomultiplier tube.

2.3 Photocatalyst measurement

A solar light simulator (model: 67005, Oriel) that simulates sunlight under one sun giving AM 1.5 G (100 mW cm^{-2}) illumination provided by a 150 W xenon arc lamp (model: 6256, Oriel) with a 400 nm cut-off filter was used as the light source. 4 mg of $Sn_{1-x}Ag_xS_2$ photocatalyst was added into 40 ml of MB aqueous solution in a beaker with an initial concentration of 10 mg l^{-1}. The vertical distance from the lamp head to the liquid surface was ~8 cm. Before starting light irradiation, the photocatalyst was added into the MB solutions under magnetic stirring. Then, the mixture was kept in the dark for 1 h to establish an adsorption/desorption equilibrium under stirring. After that, the solar light was irradiated on the surface of the solution and the instant MB concentration was monitored every 10 min by measuring the light absorption intensity at 664 nm using a UV–vis spectrophotometer (DR/4000U spectrophotometer, HACH). Each experiment was repeated twice. The degradation efficiency is calculated by using the following equation:

$$\eta = (C_0 - C)/C_0 \times 100\% \quad (1)$$

and the photocatalytic degradation rate of organic dyes followed the Langmuir–Hinshelwood mechanism in eqn (2):

$$\ln(C_0/C) = k_{app} \quad (2)$$

where k_{app} is the apparent rate constant of pseudo-first-order, t is the irradiation time, and C_0 and C are the initial and instant residual concentration of the MB solution, respectively. To study the stability of the $Sn_{1-x}Ag_xS_2$ photocatalyst, MB degradation experiments were carried out on a recycled $Sn_{1-x}Ag_xS_2$ sample. The used $Sn_{1-x}Ag_xS_2$ photocatalysts were washed with ethanol and water several times, then dried at 60 °C overnight.

3. Results and discussion

The crystallinity of pristine SnS_2, and $Sn_{1-x}Ag_xS_2$ with various dopant concentrations is studied by powder XRD. As shown in Fig. 1, all the diffraction peaks of pristine SnS_2 can be indexed to hexagonal berndtite SnS_2 with lattice parameters of

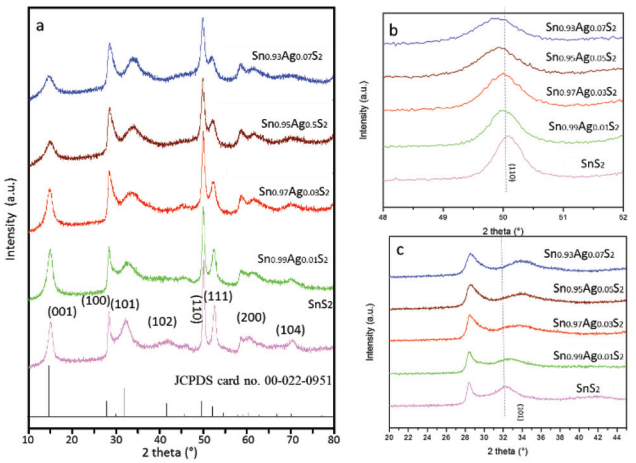

Fig. 1 (a) Powder XRD patterns of pristine SnS_2, and $Sn_{1-x}Ag_xS_2$ with various dopant concentrations, (b) (110) and (c) (101) peaks of pristine SnS_2, and $Sn_{1-x}Ag_xS_2$ with various dopant concentrations.

a = 3.640 Å, c = 5.866 Å. It is also observed, compared to the standard pattern, that the peaks for the as-prepared pristine SnS_2 tend to shift to higher 2θ angles. For example, $2\theta_{(001)}$ = 15.06°, $2\theta_{(101)}$ = 32.29° and $2\theta_{(110)}$ = 50.09° for the as-prepared pristine SnS_2, while $2\theta_{(001)}$ = 15.03°, $2\theta_{(101)}$ = 32.13° and $2\theta_{(110)}$ = 49.96° for the standard pattern, indicating shrunken lattice parameters due to ions tracked by the surfactant through nucleation and crystal growth.[26] As shown in the XRD spectrum of $Sn_{1-x}Ag_xS_2$, no formation of a new phase is observed after doping with silver, illustrating the single phase and purity of the materials. Meanwhile, it is noted that, due to the decreased crystallinity, the width of all the diffraction peaks is evidently broadened with the increased doping content. With the doping content increasing, more and more Sn^{4+} ions are substituted by Ag^+ ions, and larger numbers of defects are introduced to the lattice. Therefore, lattice distortion and lattice strain are significantly intensified, which disturbs the crystallization and leads to decreased crystallinity.[27] As displayed in Fig. 1(a), the majority of the peaks from $Sn_{1-x}Ag_xS_2$ slightly shift to lower 2θ angles and this becomes more pronounced with increasing dopant content. For example, as shown in Fig. 1(b), $2\theta_{(110)}$ = 50.09°, 50.04°, 49.98°, 49.93° and 49.86° for pristine SnS_2 and $Sn_{1-x}Ag_xS_2$ (x = 0.01, 0.03, 0.05 and 0.07), indicating that Sn^{4+} ions have been partially substituted by larger Ag^+ ions, leading to the expansion of the crystalline lattice along the a axis of the hexagonal structure. However, to balance the deformation and residual stress at grain boundaries, the c axis of the crystal must deform in the other direction.[27,28] Therefore, some peak positions will shift in the opposite direction with the increased dopant content. For example, as shown in Fig. 1(c), $2\theta_{(101)}$ = 32.29°, 32.68°, 33.45°, 33.52° and 33.61° for pristine SnS_2 and $Sn_{1-x}Ag_xS_2$ (x = 0.01, 0.03, 0.05 and 0.07). The lattice parameters for hexagonal pristine SnS_2 and $Sn_{1-x}Ag_xS_2$ with various dopant concentrations are shown in Table 1. Overall, silver ions have been doped into the SnS_2 lattice, and the increased silver doping content results in intensified lattice strain and stress leading to intensified lattice distortion.

Table 1 Lattice parameters of pristine SnS_2, and $Sn_{1-x}Ag_xS_2$ with various dopant concentrations

Sample	a (Å)	c (Å)
SnS_2	3.640	5.866
$Sn_{0.99}Ag_{0.01}S_2$	3.645	5.829
$Sn_{0.97}Ag_{0.03}S_2$	3.647	5.692
$Sn_{0.95}Ag_{0.05}S_2$	3.650	5.628
$Sn_{0.93}Ag_{0.07}S_2$	3.656	5.602

The morphologies of pristine SnS_2, and $Sn_{1-x}Ag_xS_2$ with various dopant concentrations are then studied by SEM. As shown in Fig. 2(a), the pristine SnS_2 sample is composed of clusters of very fine nanoparticles with an average size of about 20 nm. Due to the binding of surfactant molecules, the surface energy of the SnS_2 nuclei centers is significantly reduced, which inhibits them from growing into flake-like 2D structures as shown in Fig. 2(f) and results in ellipsoidal nanoparticles with reduced sizes.[26,29,30] The surface morphology of $Sn_{1-x}Ag_xS_2$ with various dopant concentrations is displayed in Fig. 2(b)–(e). It is found that the average particle size is signi-

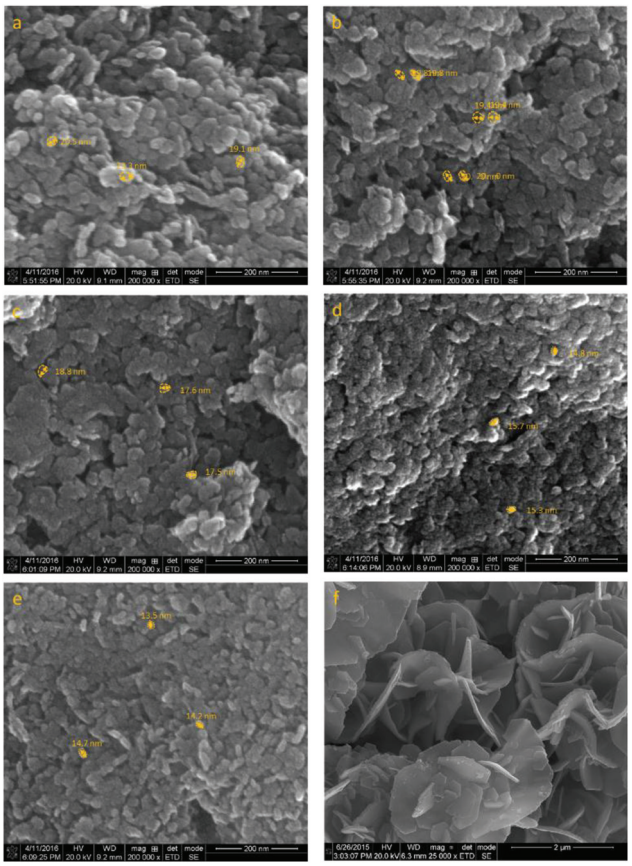

Fig. 2 SEM images of (a) pristine SnS_2, (b) $Sn_{0.99}Ag_{0.01}S_2$, (c) $Sn_{0.97}Ag_{0.03}S_2$, (d) $Sn_{0.95}Ag_{0.05}S_2$, (e) $Sn_{0.93}Ag_{0.07}S_2$ and (f) pristine SnS_2 prepared by the same method without adding surfactant.

ficantly reduced by introducing the Ag dopant. With the increased dopant concentration, the particle size decreases continuously, because the larger Ag^{+} ions residing at the boundary of the nuclei centers slow down the diffusion rate of ions which results in inhibited crystallization and reduced particle size.[31] Due to the evidently increased surface area to volume ratio, the ultra-small particle size will drive faster heterogeneous catalysis and thus lead to enhanced catalytic performance.[32–35]

The chemical states and bonding conditions of pristine SnS_2 and $Sn_{0.95}Ag_{0.05}S_2$ are studied by XPS as shown in Fig. 3. It can be observed that, besides C and O from surface contamination, only Sn and S peaks exist in the survey spectrum of pristine SnS_2, indicating the purity of the material. As displayed in Fig. 3b, the peaks at 493.4 eV and 485.0 eV in the Sn 3d region of pristine SnS_2 indicate a 3d doublet peak splitting of 8.4 eV, showing the 4^{+} state of Sn without any impurities.[36] It is clearly shown in Fig. 3b and c that Ag doping causes an obvious peak shift of both Sn 3d and S 2p to lower energy regions, demonstrating the formation of Sn–Ag–S bonding and Ag–S bonding in the doping process. As shown in Fig. 3d, the peaks at 372.1 eV (Ag $3d_{3/2}$) and 366.1 eV (Ag $3d_{5/2}$) indicate the formation of Ag ions.[37,38]

TEM with selected-area electron diffraction (SAED) is performed to confirm the crystallinity and structure of the $Sn_{1-x}Ag_xS_2$ samples. As shown in Fig. 4(a), $Sn_{0.95}Ag_{0.05}S_2$ nanoparticles have a diameter of ~15 nm with uniform size. It can be seen that introducing the Ag dopant has no effect on the morphology of the SnS_2 nanoparticles and the sample is only composed of one type of particle without the formation of any second phase. Fig. 4(b) displays the HRTEM image of $Sn_{0.95}Ag_{0.05}S_2$ with the lattice fringe spacings of 3.13 Å and 5.98 Å indexed to the (100) and (001) planes of hexagonal $Sn_{0.95}Ag_{0.05}S_2$, respectively. In addition, as observed in the inset of Fig. 4(b), the SAED pattern is in good agreement with the XRD results in Fig. 1.

The optical properties of pristine SnS_2 and $Sn_{1-x}Ag_xS_2$ with various dopant concentrations are investigated by diffuse reflectance spectroscopy (DRS) from 300 nm to 800 nm. As shown in Fig. 5, the absorption edge of pristine SnS_2 appears at the shortest wavelength; after silver doping, the absorbance shoulder apparently shifts to the longer wavelength regions, indicating an evident narrowing of the band gap. By increasing the Ag content, the edge wavelength keeps increasing and extends to the longest value when x is increased to 0.07. The band gap energy values are determined by using a Tauc plot, as shown in Fig. 6. By plotting $(\alpha h\nu)^2$ *vs.* photon energy ($h\nu$), the band gap energy can be estimated by using the equation:

$$(\alpha h\nu)^2 = A(h\nu - E_g)$$

where α is the absorption coefficient, $h\nu$ is photon energy, E_g is the band gap energy, and A is the slope constant. The absorbance coefficient (α) is calculated by the Manifacier model. By extracting the straight line portion of the graph and extending it to zero absorption on the photon energy axis, the band gap energy is determined by taking the intercept. As summarized in Table 2, the band gap of pristine SnS_2 is 2.04 eV. By doping it with 1% Ag, the band gap is significantly narrowed to 1.86 eV and keeps decreasing with the increased Ag content

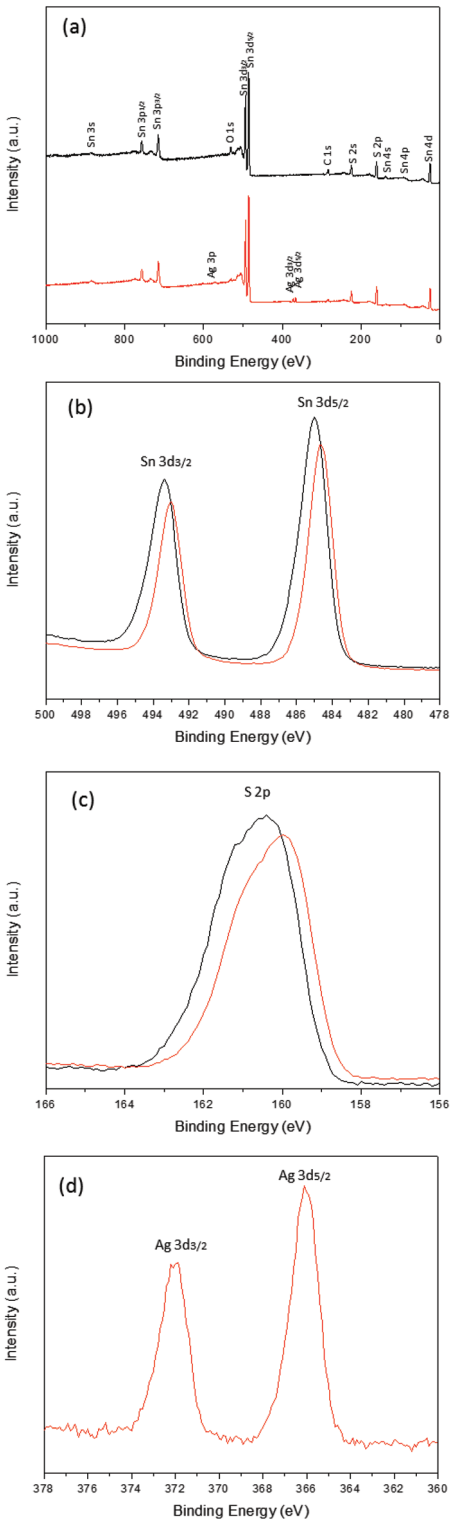

Fig. 3 XPS (a) survey spectra, and (b) Sn 3d, (c) S 2p and (d) Ag 3d core level spectra of pristine SnS_2 (black) and $Sn_{0.95}Ag_{0.05}S_2$ (red).

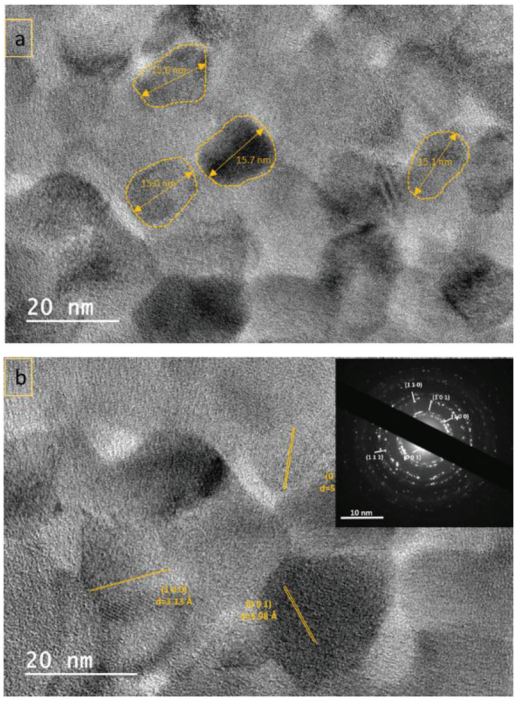

Fig. 4 (a) TEM image and (b) HRTEM image of $Sn_{0.95}Ag_{0.05}S_2$. Inset: the corresponding SAED pattern.

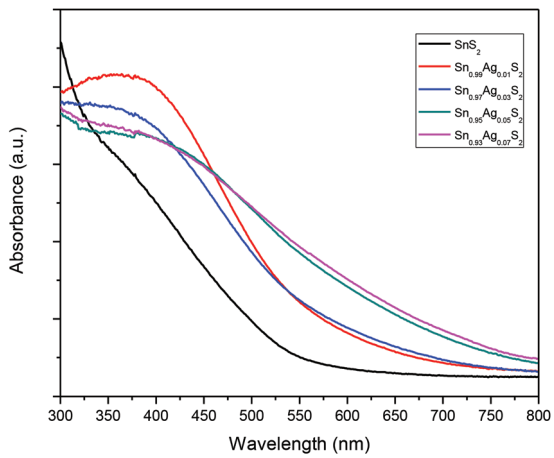

Fig. 5 UV-Vis absorption spectra of pristine SnS_2, and $Sn_{1-x}Ag_xS_2$ with various dopant concentrations.

until x = 0.05 (1.52 eV), indicating a significantly narrowed band gap, which can efficiently red shift the wavelength range for the photocatalyst's electron activation. However, further increasing the doping content to 7% does not decrease the band gap and the band gap of $Sn_{0.93}Ag_{0.07}S_2$ is maintained at 1.52 eV. This phenomenon occurs because excessive Ag cannot enter the lattice of the crystals or further alter the band gap due to the intensified lattice disordering with the increased doping content.

As shown in Fig. 7, the overall degradation rate of methylene blue (MB) upon pristine SnS_2 and $Sn_{1-x}Ag_xS_2$ with various

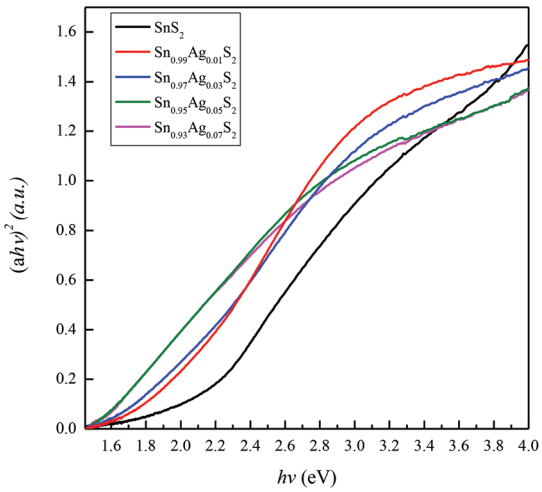

Fig. 6 $(\alpha h\nu)^2$ *vs.* photon energy ($h\nu$) for pristine SnS_2, and $Sn_{1-x}Ag_xS_2$ with various dopant concentrations.

dopant concentrations is evaluated by measuring the concentration of MB in an aqueous solution under dark conditions and visible light irradiation. It can be seen that all the photocatalysts reach an adsorption/desorption equilibrium in 45 min and further extending the dark time does not increase the adsorption amount. It is found that the increase in the Ag dopant content effectively enhances the overall degradation efficiency. The final degradation rates of MB under visible light after 60 min of irradiation over pristine SnS_2, and $Sn_{1-x}Ag_xS_2$ with x = 0.01, 0.03, 0.05 and 0.07 are 63.88%, 70.96%, 82.34%, 96.81% and 96.75%, respectively, compared to its initial concentration. The optimal concentration of the Ag dopant is found to be 5%.

Fig. 8 displays the MB adsorption capacities of pristine SnS_2, and $Sn_{1-x}Ag_xS_2$ with various dopant concentrations in the dark. As shown in Fig. 7, the adsorption/desorption equilibrium is achieved within 45 min for all the samples. It is observed that the adsorption capacities increase with the increased Ag dopant content. The pristine SnS_2 only adsorbs 45.07% of the MB in the solution, while the adsorption ratio increases to 51.48% after 1% Ag doping. By increasing the Ag content, the adsorption capacity increases continuously and reaches 87.41% for $Sn_{0.93}Ag_{0.07}S_2$, indicating that Ag doping effectively increases the affinity of MB molecules towards the photocatalyst. The enhanced adsorption is driven by the increased surface area contributed by the significantly reduced particle size achieved through Ag doping.

The photocatalytic activities of pristine SnS_2 and $Sn_{1-x}Ag_xS_2$ with various dopant concentrations are evaluated by measuring the decomposition of MB in an aqueous solution under visible light irradiation. It can be seen in Fig. 9 that the increase of the Ag dopant concentration from 1% to 5% effectively enhances the degradation efficiency. However, further increasing the Ag doping decreases the photocatalytic activity. To quantify the reaction kinetics of MB photocatalytic degradation, a pseudo-first order model for low dye concentrations

Table 2 Calculated band gaps of pristine SnS_2, and $Sn_{1-x}Ag_xS_2$ (x = 0.01, 0.03, 0.05, 0.07)

Samples	SnS_2	$Sn_{0.99}Ag_{0.01}S_2$	$Sn_{0.97}Ag_{0.03}S_2$	$Sn_{0.95}Ag_{0.05}S_2$	$Sn_{0.93}Ag_{0.07}S_2$
Band gap	2.04 eV	1.86 eV	1.73 eV	1.52 eV	1.52 eV

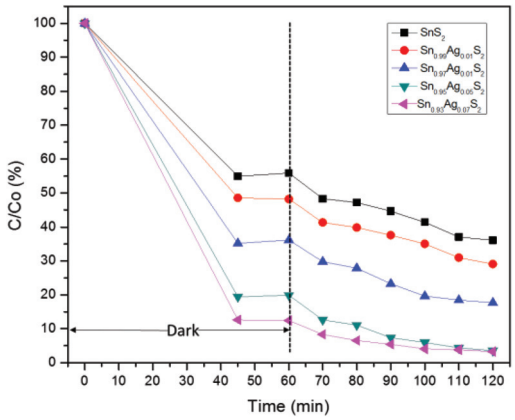

Fig. 7 Time profile of C/C_0 for methylene blue (MB) under visible light irradiation in the presence of pristine SnS_2, and $Sn_{1-x}Ag_xS_2$ with various dopant concentrations, where C_0 and C are the initial and instant concentrations of the MB aqueous solution, respectively.

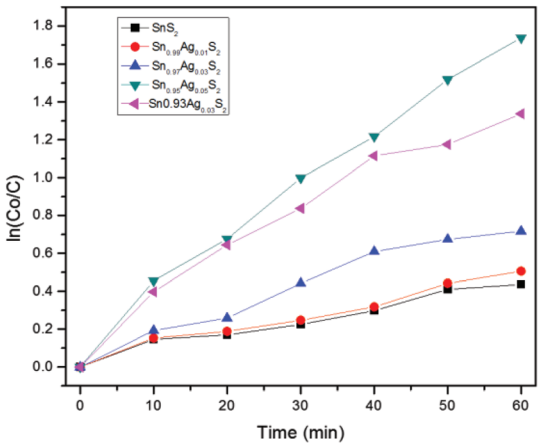

Fig. 9 Photodegradation kinetic curves of MB photodegradation in the presence of pristine SnS_2, and $Sn_{1-x}Ag_xS_2$ with various dopant concentrations.

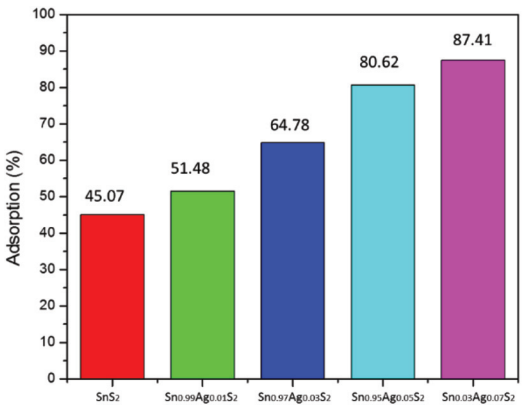

Fig. 8 Methylene blue adsorption capacity of pristine SnS_2, and $Sn_{1-x}Ag_xS_2$ with various dopant concentrations.

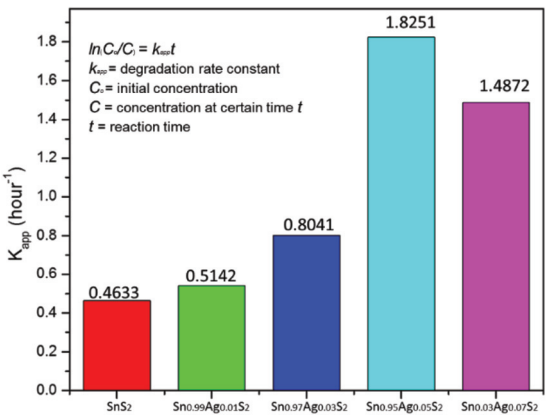

Fig. 10 The apparent rate constants (k_{app}) of MB degradation under visible-light irradiation in the presence of pristine SnS_2, and $Sn_{1-x}Ag_xS_2$ with various dopant concentrations.

is applied: $\ln(C_0/C) = k_{app}t$, where C_0 and C are the concentrations of dye in the aqueous solution at the initial time t_0 and irradiation time t respectively, and k_{app} is the pseudo-first order rate constant.[39] As plotted in Fig. 10, the calculated degradation rate constants of MB under visible light over pristine SnS_2, and $Sn_{1-x}Ag_xS_2$ with x = 0.01, 0.03, 0.05 and 0.07 are 0.4633, 0.5142, 0.8041, 1.8251 and 1.4872 hour^{-1}, respectively. $Sn_{0.95}Ag_{0.05}S_2$ is demonstrated to have the highest k_{app}. The mechanism of the photocatalytic reaction has three steps. First, electrons in the photocatalyst are excited into the conduction band by incident photons and holes are left in the valence band. Second, the excited electrons and holes migrate to the catalyst surface. Third, the oxygen donors from the dyes react with the surface electrons to form $^{\bullet}O_2^-$, while H_2O serves as an electron donor to react with holes to form $^{\bullet}OH$ and decompose the dyes as a result. Through Ag doping, the band gap is effectively narrowed, thus significantly red shifting the wavelength range for the photocatalyst's electron activation and increasing the solar light adsorption efficiency in step 1 as a result. Additionally, the doping of Ag^+ ions introduces defects into the crystal, leading to increased charge carrier density.[17,40] Therefore, electron and hole transfers in step 2 are largely accelerated and electron–hole recombination is effectively suppressed by the enhanced grain boundaries. Meanwhile, due to the evidently increased surface area to

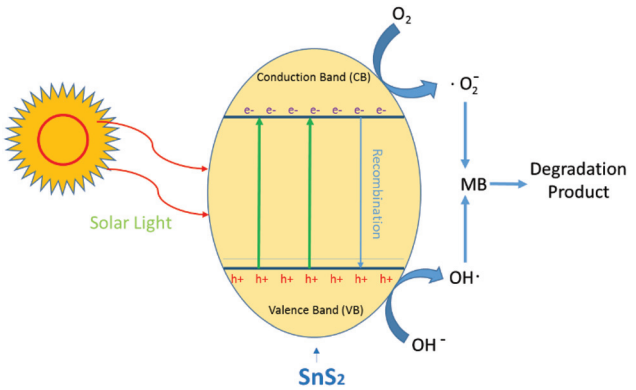

Fig. 11 Schematic mechanism of the SnS_2 photocatalyst.

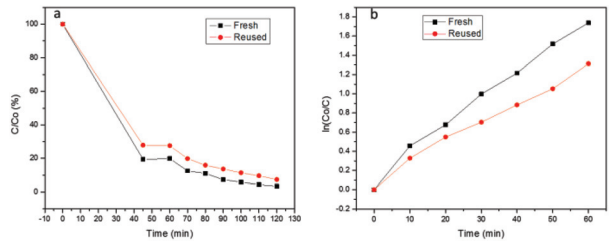

Fig. 12 (a) Time profile of C/C_0 for methylene blue (MB) under visible light irradiation, (b) photodegradation kinetic curves of MB photodegradation in the presence of fresh and reused $Sn_{0.95}Ag_{0.05}S_2$.

volume ratio, the heterogeneous catalytic reaction is effectively enhanced in step 3. However, when the doping Ag content increases to 7%, the photocatalytic performance is not further increased. This is because lattice disorder is intensified with the increased doping content. Over a certain concentration, the strong lattice distortion and strain will finally disturb crystal growth and excessive Ag cannot enter the lattice or further alter the band gap. In addition, the formation of tiny catalytic inert Ag_2S may block the active surface of $Sn_{1-x}Ag_xS_2$. Therefore, the mechanism of MB photodegradation is illustrated in Fig. 11. Due to the narrowed band gap through Ag doping, SnS_2 can be excited by solar light more easily to produce electron–hole pairs. Simultaneously, electron–hole recombination is suppressed owing to the direct oxidization of MB. To study the stability of the photocatalyst, MB degradation experiments were carried out on a recycled $Sn_{0.95}Ag_{0.05}S_2$ sample. As shown in Fig. 12, the reused $Sn_{0.95}Ag_{0.05}S_2$ photocatalyst has an overall degradation rate of 92.59% and a k_{app} of 1.3325 hour^{-1}, which exhibits no significant performance loss, indicating $Sn_{0.95}Ag_{0.05}S_2$ maintains a good stability.

4. Conclusions

In this work, a $Sn_{1-x}Ag_xS_2$ photocatalyst with varied Ag doping content is synthesized through a facile one-step hydrothermal method. The resultant $Sn_{1-x}Ag_xS_2$ shows a significantly narrowed band gap with increasing Ag doping content which reaches a minimum of 1.52 eV at 5%. Further increasing the Ag concentration does not further decrease the band gap. The photocatalytic activity of the $Sn_{1-x}Ag_xS_2$ nanoparticles is studied by the degradation of methylene blue (MB) dye under visible light irradiation. Through increasing the Ag dopant concentration, the wavelength range for the photocatalyst's electron activation is red shifted evidently and the solar light adsorption efficiency is increased effectively. In addition, due to the increased charge carrier density, electron and hole transfers are largely accelerated. Meanwhile, because of the increased surface area to volume ratio, heterogeneous catalysis is facilitated. The optimal concentration of the Ag dopant is found to be 5%. Because the lattice disorder is intensified with the increased doping content, excessive Ag cannot enter the lattice of the crystal and tiny catalytic inert Ag_2S blocks the active surface of $Sn_{1-x}Ag_xS_2$, further increasing the Ag dopant content to 7% does not further improve its photocatalytic performance. This study indicates that a proper amount of Ag doping can effectively increase the photocatalytic performance of SnS_2 and will promote the commercialization of such photocatalysts in the photocatalytic degradation of organic compounds.

Acknowledgements

The authors would like to acknowledge the Chevron Innovative Research Fund (CIRS) sponsored by Chevron Incorporation and Louisiana State University (LSU) and the Graduate Enrichment Award from LSU for the financial support of this project. We also acknowledge the Shared Instrumentation Facilities (SIF) in LSU for the use of their SEM, XRD and TEM apparatus.

References

1 C. R. Nony, M. C. Bowman, T. Cairns, L. K. Lowry and W. P. Talos, *J. Anal. Toxicol.*, 1980, **4**, 132–140.
2 R. B. Haveland-Smith, R. D. Combes and B. A. Bridges, *Mutat. Res., Genet. Toxicol. Test.*, 1981, **88**, 1–15.
3 X. Li, J. Zhu and H. Li, *Appl. Catal., B*, 2012, **123–124**, 174–181.
4 M. A. Rauf and S. S. Ashraf, *Chem. Eng. J.*, 2009, **151**, 10–18.
5 X. Luan and Y. Wang, *Mater. Sci. Semicond. Process.*, 2014, **25**, 43–51.
6 X. Luan, M. T. Gutierrez Wing and Y. Wang, *Mater. Sci. Semicond. Process.*, 2015, **30**, 592–598.
7 J. Zhang, S. Li, P. Yang, W. Que and W. Liu, *Sci. China Mater.*, 2015, **58**, 785–790.
8 R. Hao, B. Jiang, M. Li, Y. Xie and H. Fu, *Sci. China Mater.*, 2015, **58**, 363–369.
9 Y. C. Zhang, Z. N. Du, K. W. Li, M. Zhang and D. D. Dionysiou, *ACS Appl. Mater. Interfaces*, 2011, **3**, 1528–1537.

10 H. Wang, W. Chen, J. Zhang, C. Huang and L. Mao, *Int. J. Hydrogen Energy*, 2015, **40**, 340–345.
11 W. Xu, Z. Xie, X. Cui, K. Zhao, L. Zhang, G. Dietrich, K. M. Dooley and Y. Wang, *ACS Appl. Mater. Interfaces*, 2015, **7**, 22533–22541.
12 X. Cui, W. Xu, Z. Xie and Y. Wang, *J. Mater. Chem. A*, 2016, **4**, 1908–1914.
13 X. Cui, W. Xu, Z. Xie and Y. Wang, *Electrochim. Acta*, 2015, **186**, 125–132.
14 J. Yu, C.-Y. Xu, F.-X. Ma, S.-P. Hu, Y.-W. Zhang and L. Zhen, *ACS Appl. Mater. Interfaces*, 2014, **6**, 22370–22377.
15 S. Park, J. Park, R. Selvaraj and Y. Kim, *J. Ind. Eng. Chem.*, 2015, **31**, 269–275.
16 J. Li, T. Wang and X. Du, *Sep. Purif. Technol.*, 2012, **101**, 11–17.
17 R. Chauhan, A. Kumar and R. P. Chaudhary, *Appl. Surf. Sci.*, 2013, **270**, 655–660.
18 X. Cui, Z. Xie and Y. Wang, *Nanoscale*, 2016, **8**, 11984–11992.
19 X. Cui, A. D. Zdunek, G. Jursich and C. G. Takoudis, *ECS J. Solid State Sci. Technol.*, 2015, **4**, P429–P435.
20 W. Xu, X. Cui, Z. Xie, G. Dietrich and Y. Wang, *ChemElectroChem*, 2016, **3**, 1098–1106.
21 W. Xu, Z. Xie, X. Cui, K. Zhao, L. Zhang, L. Mai and Y. Wang, *J. Mater. Chem. A*, 2016, **4**, 3735–3742.
22 Z. Wang and J. J. Spivey, *Appl. Catal., A*, 2015, **507**, 75–81.
23 J. Liu, Y. Zhao, J. Liu, S. Wang, Y. Cheng, M. Ji, Y. Zhou, M. Xu, W. Hao and J. Zhang, *Sci. China Mater.*, 2015, **58**, 693–703.
24 Y. Liu, C.-Y. Liu, Q.-H. Rong and Z. Zhang, *Appl. Surf. Sci.*, 2003, **220**, 7–11.
25 M. K. Seery, R. George, P. Floris and S. C. Pillai, *J. Photochem. Photobiol., A*, 2007, **189**, 258–263.
26 J. Gajendiran and V. Rajendran, *Adv. Nat. Sci.: Nanosci. Nanotechnol.*, 2011, **2**, 015001.
27 L. Xu and X. Li, *J. Cryst. Growth*, 2010, **312**, 851–855.
28 A. K. Singh, *J. Phys. Chem. Solids*, 2004, **65**, 1589–1596.
29 Q. Yang, K. Tang, C. Wang, D. Zhang and Y. Qian, *J. Solid State Chem.*, 2002, **164**, 106–109.
30 W. Xu, Z. Xie, X. Cui, K. Zhao, L. Zhang, G. Dietrich, K. M. Dooley and Y. Wang, *ACS Appl. Mater. Interfaces*, 2015, **7**, 22533–22541.
31 Y. W. Zhang, Y. Yang, S. Jin, C. S. Liao and C. H. Yan, *J. Mater. Sci. Lett.*, 2002, **21**, 943–946.
32 N. Kumar, A. Roy, Z. Wang, E. M. L'Abbate, D. Haynes, D. Shekhawat and J. J. Spivey, *Appl. Catal., A*, 2016, **517**, 211–216.
33 Z. Xie, Z. He, X. Feng, W. Xu, X. Cui, J. Zhang, C. Yan, M. A. Carreon, Z. Liu and Y. Wang, *ACS Appl. Mater. Interfaces*, 2016, **8**, 10324–10333.
34 Z. Wang, N. Kumar and J. J. Spivey, *J. Catal.*, 2016, **339**, 1–8.
35 G. Prieto, S. Beijer, M. L. Smith, M. He, Y. Au, Z. Wang, D. A. Bruce, K. P. de Jong, J. J. Spivey and P. E. de Jongh, *Angew. Chem., Int. Ed.*, 2014, **53**, 6397–6401.
36 M. Di Giulio, A. Serra, A. Tepore, R. Rella, P. Siciliano and L. Mirenghi, *Mater. Sci. Forum*, 1996, **203**, 143–147.
37 L. Xiaofeng, L. Linlin, Z. Wanjin and W. Ce, *Nanotechnology*, 2005, **16**, 2233.
38 K. Asami, *J. Electron Spectrosc. Relat. Phenom.*, 1976, **9**, 469–478.
39 M. Ahmad, E. Ahmed, Y. Zhang, N. R. Khalid, J. Xu, M. Ullah and Z. Hong, *Curr. Appl. Phys.*, 2013, **13**, 697–704.
40 H. Zhang, Y. Li, T. Xu, J. Wang, Z. Huo, P. Wan and X. Sun, *J. Mater. Chem. A*, 2015, **3**, 15020–15023.